Physics Letters A 374 (2010) 2709–2722

Contents lists available at ScienceDirect

Physics Letters A

www.elsevier.com/locate/pla

# Basins of attraction in a ring of overdamped bistable systems with delayed coupling

Daniel Lyons [a], Joseph M. Mahaffy [a], Antonio Palacios [a,*], Visarath In [b], Patrick Longhini [b], Andy Kho [b]

[a] Nonlinear Dynamical Systems Group, Department of Mathematics, San Diego State University, San Diego, CA 92182, USA
[b] Space and Naval Warfare Systems Center San Diego, Code 2363, 53560 Hull St, San Diego, CA 92152-5001, USA

ARTICLE INFO

*Article history:*
Received 5 January 2010
Received in revised form 20 April 2010
Accepted 21 April 2010
Available online 24 April 2010
Communicated by C.R. Doering

*Keywords:*
Coupled systems
Fluxgates
Delay
Bistability

ABSTRACT

Theoretical and experimental works reveal that coupling similar overdamped bistable systems can lead, under certain conditions that depend on the topology of connections and the number of units, to self-induced large-amplitude oscillations that emerge through a global bifurcation of heteroclinic connections between saddle-node equilibria. This critical observation has led to new mechanisms for weak (compared to the energy barrier height) signal detection and amplification. While the mathematical models and related devices governed by bistable potential functions may assume instantaneous coupling, in practice we must account for the fact that even high-speed, high-precision, circuit components can introduce a delay in the coupling signal. Thus, in this manuscript we investigate the behavior of a ring of overdamped bistable systems with delayed nearest-neighbor connections. Related work, without delay, shows that large-amplitude oscillations and nontrivial synchronous equilibria can coexist near the onset of the oscillations. Our study shows that a delay-induced Hopf bifurcation occurs from the synchronous equilibria but, generically, the small amplitude oscillations that appear are unstable. Thus, delay has the effect of decreasing the size of the basin of attraction of nontrivial synchronous equilibria, which in turn, makes the basin of attraction of the stable large-amplitude oscillations larger. Collectively, this is a positive effect because the sensor device depends mainly on large amplitude oscillations, so a small delay can make it easier to induce the device to oscillate on its own. As a "test bed", we use the model equations of a CCFM device with $N$ fluxgates. The results are, however, generic and applicable to all rings of overdamped bistable units unidirectionally coupled.



## 1. Introduction

Bistability, the attribute which indicates that two possible states of a system are possible, can be found in many physical systems, including: optical devices, Schmitt triggers, neural integrators, and ferroelectric and ferromagnetic sensors. The behavior of these, and many other systems, is governed, generically, by a gradient system of the form $\dot{x} = \nabla U(x)$, where $x(t)$ is the state variable of the device at time $t$, e.g., magnetization state, and $U(x)$ is the bistable potential function. In the absence of an external force, the state point $x(t)$ will rapidly relax to one of the two stable states, each associated with a local minimum of the potential function. Which state is actually observed depends on the actual initial conditions. In the presence of an external force, however, the system can exhibit a hysteresis loop in which the state point $x(t)$ can be induced to oscillate between the two stable states. The hysteresis behavior is normally employed in the *standard*, spectral-based [1–3], detection mechanism of small target signals (dc or low frequency signals) wherein a known periodic bias signal is applied to induce a sensor device to oscillate between two stable attractors. In the absence of a target signal, the power spectral density contains only the odd harmonics of the bias frequency. In the presence of a weak target signal, however, the potential energy function is skewed, resulting in the appearance of even harmonics. The response at the second harmonic is then used to detect and quantify the target signal.

In recent works [4,5], we have demonstrated, theoretically and experimentally, that coupling similar bistable systems can lead, under certain conditions, to self-induced oscillations that mimic the hysteresis loop of a single element. The conditions depend, mainly, on the topology of connections and the number of units. But, more importantly, since the oscillations appear without the need of an external signal, they provide an alternative signal detection scheme as well as, potentially, enhanced sensitivity. These results have been incorporated

* Corresponding author.
*E-mail address:* palacios@euler.sdsu.edu (A. Palacios).

0375-9601/$ – see front matter 
doi:10.1016/j.physleta.2010.04.060

into a "coupled core fluxgate magnetometer (CCFM)" [4] and in a "coupled electric field sensor (CEFS)" [6]. The analysis of the effects of different coupling schemes has also led to the prediction of novel cooperative behavior in a ring of coupled SQUID (Superconducting Quantum Intereference Devices) devices [7].

In this Letter we concentrate on the CCFM system as the "test-bed" to study the effects of time delay in generic formulations of coupled bistable systems. While the laboratory realization of the CCFM employs high-speed, high-precision, operational amplifiers, a comprehensive analysis of the effects of time delay is still needed. In particular, to help us understand the potential effects of delay in the signal processing module that reads out and processes the output of each individual fluxgate before it can be used to drive the dynamics of another fluxgate.

This Letter is organized as follows. In Section 2, we start with an overview of fluxgate magnetometers, which should be valuable to readers not familiar with the technology. In Section 3 we provide a description of the dynamics of the coupled bistable model equation for a CCFM without delay, comprised of an odd number $N$ of wound ferromagnetic cores. We note that $N$ (unless taken to be quite large) must be odd [4,8]. Then in Section 4 we present results of an analytic and computational study of the effects of time delay. Before we advance to the next section we wish to emphasize that the results of this Letter, while relevant to the CCFM as a "test-bed", are also applicable to almost all overdamped bistable dynamic systems.

## 2. Overview of fluxgate magnetometers

Fluxgate magnetometers [9] are considered to be the most cost-efficient magnetic field sensors for applications that require measuring relatively small magnetic fields in the 0.01 mT regime. Originally developed around 1928, today's highly specialized devices can measure magnetic fields in the range of 1–10 $\mathrm{pT}/\sqrt{\mathrm{Hz}}$ [11] for a variety of magnetic remote sensing applications [10]. In its most basic form, the fluxgate magnetometer consists of two detection coils wound around two ferromagnetic cores (usually a single core configured as an open-ended "racetrack") in opposite directions to one another [9].

The ferromagnetic core that underpins the magnetometer is hysteretic in its core magnetization response to an external magnetic field; the dynamics can be modeled via the particle-in-potential paradigm, with the potential energy function being bistable. In practice, the coercive field (roughly the deterministic switching threshold between the stable states of the energy function) can be quite high, so that the device shows little response to a target signal of amplitude far smaller than the energy barrier height. Hence, the *standard* operating mode consists of applying a known time-periodic (usually taken to be triangular or sinusoidal) bias signal, of very large amplitude, to periodically drive the core between its two stable magnetization states. In the absence of the target signal, the power spectral density of the output contains only the odd harmonics of the (known) bias frequency. In the presence of a weak (assumed near dc) target signal, however, the potential energy function is skewed, resulting in the appearance of even harmonics. The frequency response at the second harmonic is then used to detect and quantify the target signal [9,12].

In our ongoing work (on the single core fluxgate as well as the CCFM) we rely on a readout mechanism, based on a threshold crossing strategy, that consists of measuring the "residence times" of the ferromagnetic core(s) in the two stable states of the potential energy function [13]. When the potential energy function is skewed due to the presence of a target dc signal, the residence times are no longer equal. Then either their difference or ratio can be used to quantify the signal. The sensitivity of this residence times distribution (RTD) based readout has been shown [8] to increase with lowered bias frequency and amplitude. These conditions are the opposite of the requirements for enhancing sensitivity in traditional (second harmonic) readouts, so that lower onboard power as well as far simpler electronics can be implemented, with benefit, for this (time domain based) readout strategy [8].

## 3. Cooperative behavior without delay

A conventional (i.e., single core) fluxgate magnetometer can be treated as a nonlinear dynamical system by assuming the core to be approximately single-domain [13], and writing down an equation for the evolution of the (suitably normalized) macroscopic magnetization parameter $x(t) : \dot{x}(t) = -\nabla_x U(x)$ in terms of the potential energy function $U(x,t) = x^2(t)/2 - c^{-1}\ln\cosh c[x(t) + A\sin\omega t + \varepsilon(t)]$, where $c$ is a nonlinear temperature-dependent parameter, which controls the topology of the potential function: the system becomes monostable, or paramagnetic, for $c < 1$ corresponding to an increase in the core temperature past the Curie point. The overdot denotes the time-derivative, $A\sin\omega t$ is the known bias signal that switches the core dynamics between the potential minima, and $\varepsilon(t)$ is an external target signal (taken to be a dc signal throughout this treatment).

The CCFM is, then, constructed by *uni*directionally coupling $N$ (odd) wound ferromagnetic cores with cyclic boundary condition, thereby leading to the dynamics,

$$\dot{x}_i = -x_i + \tanh\big(c(x_i + \lambda x_{i+1} + \varepsilon)\big), \quad i = 1,\ldots,N \bmod N, \tag{1}$$

where $x_i(t)$ represents the (suitably normalized) magnetic flux at the output (i.e. in the secondary coil) of unit $i$, and $\varepsilon \ll U_0$ is an external dc "target" magnetic flux, $U_0$ being the energy barrier height (absent the coupling) for each of the elements (assumed identical for theoretical purposes). The parameter $\lambda$ represents the strength of coupling between $x_i$ and $x_{i+1}$. For our study we are primarily interested in $\lambda < 0$, which represents a negative feedback in the system when $N$ is odd. It is important to note [4] that the oscillatory behavior occurs even for $\varepsilon = 0$. However, when $\varepsilon \neq 0$, the oscillation characteristics change. These changes can be exploited for signal quantification purposes, the motivation for this work. We reiterate that the oscillations do *not* occur for $\lambda = 0$, due to the overdamped nature of the dynamics (1). Note the absence of the bias signal in the dynamics (1); in the coupled core system, the oscillations (corresponding to switching events in each core between the allowed stable states) are generated by the coupling and the cyclic boundary condition. In an experimental setup, there is always a power supply in the circuit to drive the electronic components that make up the device, e.g., the coupling circuit, so that the oscillations do not violate any fundamental laws. We also observe that the particle-in-potential paradigm is no longer applicable to the coupled system (1) due to the unidirectional coupling. The case of a time-periodic external magnetic flux signal has been discussed in a recent manuscript [14] and is not addressed in this Letter.

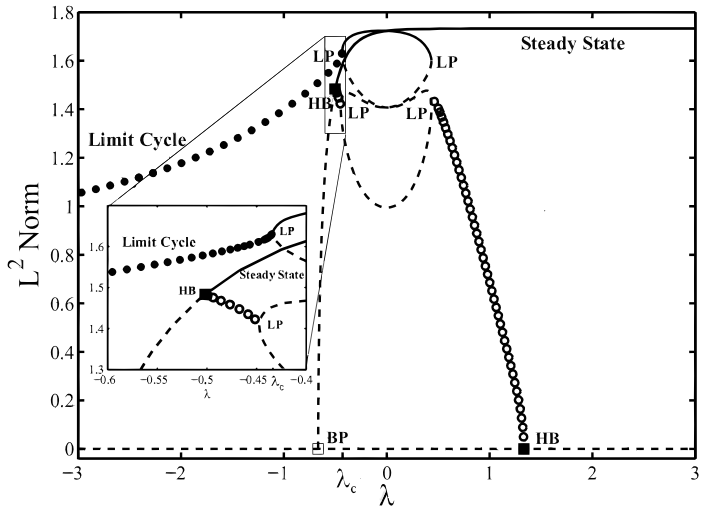


**Fig. 1.** Bifurcation diagram for a system of three identical bistable elements coupled unidirectionally and without delay. Solid (dotted) lines indicate stable (unstable) equilibrium points. Filled-in (empty) circles represent stable (unstable) periodic oscillations. (Insert) Close-up view of the region of bistability between large-amplitude oscillations and synchronous equilibria.

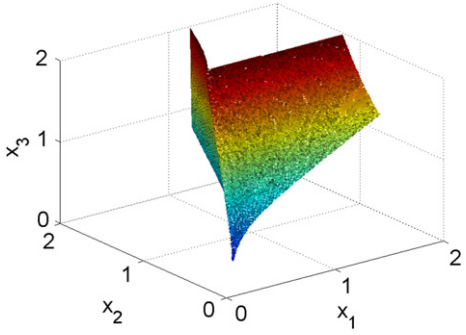


**Fig. 2.** Three-dimensional surface defining the boundary between the basins of attraction of equilibrium points and that of periodic oscillations for a coupled-core fluxgate magnetometer, see Eq. (1). Points inside the pyramid-like shape are attracted to synchronous equilibria while those outside are attracted to a global branch of large-amplitude periodic oscillations. Parameters are: $c = 3$, $\lambda = -0.44$, $N = 3$, $\varepsilon = 0.0$.

Under the above conditions, the system (1) displays oscillatory behavior with the following features [4]:

(A) The oscillations commence when the coupling coefficient exceeds a threshold value

$$\lambda_c = -\varepsilon - x_{inf} + c^{-1} \tanh^{-1} x_{inf}, \tag{2}$$

with $x_{inf} = \sqrt{(c-1)/c}$. Note that in our convention, $\lambda < 0$ (negative feedback) so that oscillations occur for $|\lambda| > |\lambda_c|$. The oscillations are non-sinusoidal, with a frequency that increases as the coupling strength decreases away from $\lambda_c$. For $\lambda > \lambda_c$, however, the system quickly settles into one of its steady states, regardless of the initial conditions. The same result ensues if $N$ is even, or if the coupling is bidirectional. For values of $\lambda$ slightly less than $\lambda_c$, there is a small interval $\lambda_{HB} \leqslant \lambda \leqslant \lambda_c$ where global oscillations and synchronous equilibria of the form $(x_1, \ldots, x_N) = (\bar{x}, \ldots, \bar{x})$ can coexist. This interval is the region of parameter space where we are interested in studying the effects of delayed coupling.

The bifurcation diagram for the $N = 3$ case is shown in Fig. 1. It was generated with the aid of the continuation package AUTO [15]. Filled-in circles represent stable oscillations, they emerge via an infinite-period *global* bifurcation that coincides with the creation of a heteroclinic cycle that connects multiple saddle-point equilibria. At birth the oscillations are fully grown due to the global nature of the bifurcation. As $\lambda$ approaches $\lambda_c$ (from the left), so that the strength of the negative feedback is reduced, the oscillation period lengthens and finally becomes infinite at $\lambda = \lambda_c$, when the heteroclinic cycle appears. Empty circles describe unstable oscillations, they all appear via local Hopf bifurcations (labeled HB), so their amplitude increases as a square-root law of the distance from the bifurcation point. Solid (dotted) lines depict stable (unstable) equilibrium points. In particular, the equilibrium points that appear at the pitchfork bifurcation point, labeled B, are all *synchronous*, i.e., of the form $(x_1, x_2, x_3) = (\bar{x}, \bar{x}, \bar{x})$. A close-up view of the interval of bistability of large amplitude oscillations and stable synchronous equilibria is also included. The four branches of unstable equilibria that appear via saddle-node bifurcations (labeled LP) correspond to nonsynchronous equilibria. Collectively, there are fifteen equilibrium points: three synchronous equilibria, including the trivial solution, and twelve nonsynchronous equilibrium points. The surface shown in Fig. 2 depicts the boundary between the basin of attraction of the synchronous equilibria and the large amplitude periodic oscillations. Initial conditions inside the pyramid-like shape are attracted to equilibrium points, while those outside are attracted to the large-amplitude oscillations. Observe that the size of the basin of attraction of the stable (nontrivial synchronous) equilibrium point gets larger as initial conditions move away from the origin.

(B) The individual oscillations (in each elemental response) are separated in phase by $2\pi/N$, and have period

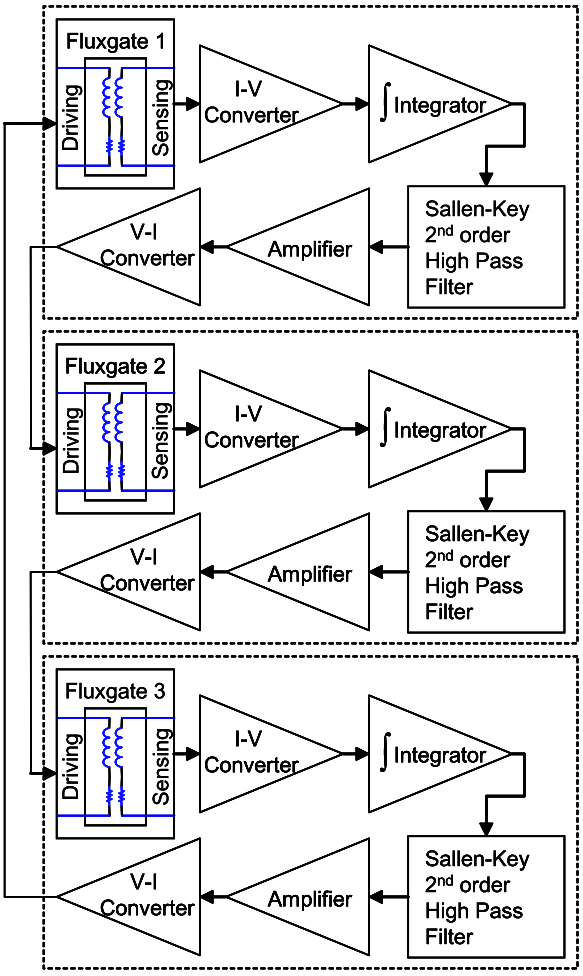


**Fig. 3.** Block diagram of CCFM.

$$T_i = \frac{N\pi}{\sqrt{cx_{inf}}}\left(\frac{1}{\sqrt{\lambda_c - \lambda}} + \frac{1}{\sqrt{\lambda_c - \lambda + 2\varepsilon}}\right), \tag{3}$$

which shows a characteristic dependence on the inverse square root of the bifurcation "distance" $\lambda_c - \lambda$, as well as the target signal $\varepsilon$. These oscillations can be experimentally produced at frequencies ranging from a few Hz to high kHz.

(C) The *summed* output oscillates at period $T_+ = T_i/N$ and its amplitude (as well as that of each elemental oscillation) is *always supra* threshold, i.e., the emergent oscillations are strong enough to drive the core between its saturation states, *eliminating* the need to apply an additional bias signal for this purpose, as is done in single-core magnetometers. Increasing $N$ changes the frequency of the individual elemental oscillations, but the frequency of the summed response is seen to be independent of $N$.

### 3.1. Experimental design

We now turn to a description of the experiments, see Fig. 3, carried out on a 3-fluxgate setup. The PCB (printed circuit board) technology based cores [8] are made of Cobalt-based Metglas 2714A material, and each is sandwiched between two sheets of PCB material. The sides of the PCB sheets that face away from the core material are printed with copper wirings to form the windings for the driving and sensing coils. Solder is used to fuse the two sheets together to complete the circuit for the windings. The cores are then coupled through electronic circuits where the (voltage) readout of one fluxgate signal (i.e., the derivative signal of the flux detected by the sensing coil) is amplified by a voltage amplifier with a very high impedance, which also trims out any dc signal in the output. Following this, the signal is passed through a "leaky" integrator to convert the derivative signal seen by the sensing coil back to the "flux" form so that the experimental system closely conforms to the model (1).

Typically, the integrator output contains a dc component that must be removed before the signal is passed to the other fluxgates. This is accomplished by employing a Sallen–Key second-order high pass filter immediately after the integrator. The signal then passes through an amplifier to achieve adequate gain to drive the adjacent fluxgate. After this, the signal passes through a voltage-to-current converter (V–I converter) in its final step to drive the primary coil of the adjacent fluxgate. The setup repeats for the remaining two fluxgates and all values of the coupling circuit parameters are closely matched from one set to the other.

Although high speed, high precision, operational amplifiers are carefully chosen for the coupling circuit, these components might still introduce small time delays that can alter the dynamics of the coupled overdamped system, and ultimately, the performance of the sensor device. Thus, we seek to understand more precisely what those effects are and what are the implications for the design and operation of sensor devices governed by coupled overdamped systems.

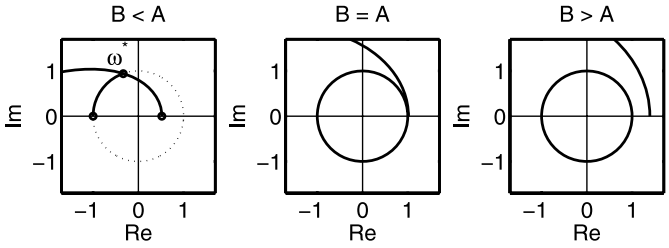


**Fig. 4.** Graphical representation of the solution set of Eq. (7) with $N = 3$.

## 4. Effects of delay

### 4.1. Model equations

We now investigate the behavior of an $N$-dimensional ($N$ odd for negative feedback) unidirectionally coupled ring of overdamped bistable systems with delayed nearest-neighboor connections. As a test case, we use the model equations (1) of a CCFM device with $N$ fluxgates:

$$\dot{x}_i(t) = -x_i(t) + \tanh\big(c\big(x_i(t) + \lambda x_{i+1}(t-\tau_i) + \varepsilon\big)\big), \tag{4}$$

where $i = 1, 2, \ldots, N \bmod N$ and $\tau_1, \tau_2, \ldots, \tau_N$, denote the corresponding delays in the connectivity scheme. Recall that we are primarily interested in the case where $\lambda < 0$, which is a negative feedback system. We make the following change of variables to create a single delayed term with $\tau = \tau_1 + \tau_2 + \cdots + \tau_N$

$$y_1(t) = x_1(t), \qquad y_2(t) = x_2(t-\tau_1), \qquad \ldots, \qquad y_N(t) = x_N\big(t - (\tau_1 + \cdots + \tau_{N_1})\big).$$

The resulting system of equations is given by

$$\begin{aligned}
\dot{y}_1(t) &= -y_1(t) + f_1\big(y_1(t), y_2(t)\big),\\
\dot{y}_2(t) &= -y_2(t) + f_2\big(y_2(t), y_3(t)\big),\\
&\vdots\\
\dot{y}_N(t) &= -y_N(t) + f_N\big(y_1(t-\tau), y_N(t)\big),
\end{aligned} \tag{5}$$

where $f_i(y_i(t), y_{i+1}(t)) = \tanh(c(y_i(t) + \lambda y_{i+1}(t) + \varepsilon))$, $i = 1, \ldots, N \bmod N$.

### 4.2. Hopf bifurcation analysis

We now wish to investigate the stability properties of the *synchronous* equilibria of the transformed system (5), which we denote by $(y_1, \ldots, y_N) = (\bar{y}, \ldots, \bar{y})$. The linearization of (5) with respect to such synchronous equilibrium solution has the form

$$\begin{bmatrix} \dot{y}_1(t) \\ \vdots \\ \dot{y}_N(t) \end{bmatrix} = \begin{bmatrix} A & B & 0 & \ldots 0 \\ 0 & A & B & \ldots 0 \\ \vdots & & & \\ 0 & 0 & 0 & \ldots A \end{bmatrix} \begin{bmatrix} \dot{y}_1(t) \\ \vdots \\ \dot{y}_N(t) \end{bmatrix} + \begin{bmatrix} 0 & 0 & 0 & \ldots 0 \\ 0 & 0 & 0 & \ldots 0 \\ \vdots & & & \\ C & 0 & 0 & \ldots 0 \end{bmatrix} \begin{bmatrix} \dot{y}_1(t-\tau) \\ \vdots \\ \dot{y}_N(t-\tau) \end{bmatrix}$$

where $A = \partial f_i(\bar{y}, \bar{y})/\partial y_i - 1$, $B = \partial f_i(\bar{y}, \bar{y})/\partial y_{i+1}$, and $C = \partial f_N(\bar{y}, \bar{y})/\partial y_1$. Because we are primarily interested in the negative feedback system, we assume $\partial f_i/\partial x_j < 0$ for $i \neq j$. Then direct calculations show that $-1 < A < 0$ and $-1 < B < 0$. As usual, we attempt to find solutions of the form $\mathbf{y}(t) = \boldsymbol{\xi} e^{\sigma t}$, with $\mathbf{y} = (y_1, y_2, \ldots, y_N)^T$. In particular, we are interested in nontrivial *synchronous* equilibria of the form $(\bar{y}_1, \bar{y}_2, \ldots, \bar{y}_N) = (\bar{y}, \ldots, \bar{y})$. Note from Fig. 1 that there are exactly two nontrivial synchronous equilibria $(\bar{y}, \ldots, \bar{y})$ and $(-\bar{y}, \ldots, -\bar{y})$. In both cases the characteristic polynomial reduces to:

$$(\sigma - A)^N = B^N e^{-\sigma\tau}, \tag{6}$$

where $\sigma$ represents the eigenvalues of the linearized system. We are interested in stability changes of the synchronous equilibria that may lead to small amplitude oscillations via a Hopf bifurcation. Those changes can only occur when $\sigma = \omega i$. Substituting this Hopf bifurcation condition in (6), we get

$$\frac{(A - \omega i)^N}{B^N} = -e^{-\omega\tau i}. \tag{7}$$

The left-hand side of (7) represents a complex-valued curve $\mathcal{C}_N(\omega)$ parametrized by $\omega$ while the right-hand side describes the unit circle in the complex plane, parametrized also by $\omega$ and by the delay $\tau$. For $\tau > 0$, as $\omega$ increases (starting at zero) the right-hand term traces the unit circle $S^1$ clockwise starting at the point $(-1, 0)$, as is shown in Fig. 4(left) for the particular case of $N = 3$.

Simultaneously, the left-hand curve $\mathcal{C}_N(\omega)$ traverses the complex plane counter-clockwise starting at the point $(A^N/B^N, 0)$. When $B < A$ this starting point is in the interval $(0 < A^N/B^N < 1, 0)$, and since the magnitude and angle of points traversed along $\mathcal{C}_N$ are continuously monotonically increasing and unbounded, then by continuity there is a critical value $\omega^*$ at which both the circle $S^1$ and

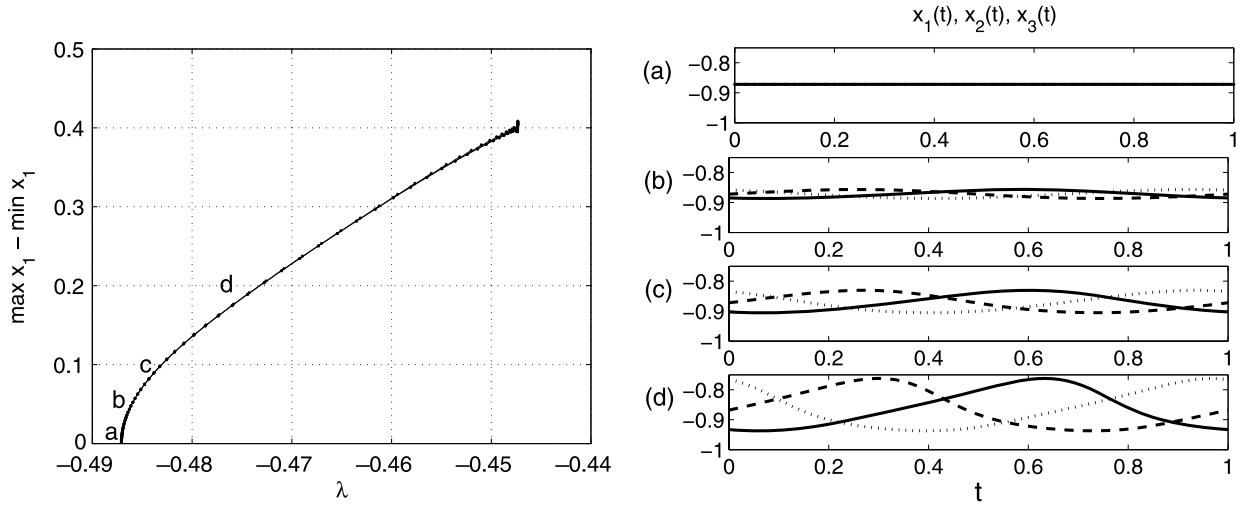


**Fig. 5.** (Left) One parameter bifurcation diagram of a branch of periodic oscillations that emerge via a delay-induced Hopf bifurcation. (Right) Time-series solutions of the oscillations at four distinct values of coupling strength marked $a$, $b$, $c$, $d$ on the bifurcation diagram to the left. Parameters are: $c = 3$, $\varepsilon = 0$, $\tau = 2$.

$\mathcal{C}_N$ intersect. At $\omega = \omega^*$, the point of intersection on $S^1$ corresponds to a critical angle $\theta_c$ measured from the starting point $(-1, 0)$. The critical delay $\tau_c$ producing the Hopf bifurcation satisfies $\tau_c = \theta_c/\omega^*$. This critical delay corresponds to the solution of (7) at the Hopf bifurcation. This type of analysis based on the Argument principle from complex analysis has been used for systems of delay differential equations with negative feedback and a similar structure to (5), as seen in [16,17]. By the periodicity of $e^{i\omega\tau}$, there are infinitely many solutions of (7), but other solutions produce larger values of $\tau$, which are unstable. The critical value $\omega^*$ can be found analytically by noticing that both sides of (7) are complex-valued expressions, which are equal only when their magnitudes and angles are identical, this produces the polynomial

$$\left(w^2 + A^2\right)^N = B^{2N},$$

whose solution $\omega^*$ yields the desired eigenvalue for the delayed-induced Hopf bifurcation point.

When $B = A$, see Fig. 4(center), the point $(A^N/B^N, 0)$ has moved to $(1, 0)$ but the right-hand side term is still at $(-1, 0)$, so as soon as $\omega$ increases the point $(A^N/B^N, 0)$ separates away from the circle due to the monotonic nature of $\mathcal{C}_N$, thus there is no solution. Similarly, when $B > A$, Fig. 4(right), the starting point $(A^N/B^N, 0)$ is already separated from the unit circle and so there is no solution either.

The branch of delay-induced oscillations terminates at a regular Hopf bifurcation from the synchronous equilibrium with $\tau = 0$. To find this bifurcation point we note that when $\tau = 0$ the linearized matrix $L$ becomes cyclic, with the eigenvectors space spanned by

$$V_j = \left\{\left[v, \zeta^j v, \zeta^{2j} v, \ldots, \zeta^{(N-1)j} v\right]\colon\ v \in R\right\},$$

where $\zeta = e^{2\pi/N}$. Direct calculations yield $L \cdot V_j = (A + \zeta^j B)V_j$. Hence the eigenvalues of $L|V_j$ are those of $A + \zeta^j B = A + \cos(2\pi j/N)B + B\sin(2\pi j/N)i$. It follows that a regular Hopf bifurcation occurs when

$$B = -\frac{1}{\cos(2\pi/N)}A, \tag{8}$$

which in the particular case of $N = 3$ it yields $B = 2A$.

Fig. 5(left) depicts a one-parameter bifurcation diagram of a branch of periodic solutions that emerges from a delay-induced Hopf bifurcation at $\lambda_c = -0.4871$ and $\tau_c \approx 2.0$, for a CCFM system with $N = 3$ and $c = 3$. The diagram was generated numerically with the aid of DDE-BIFTOOL [18], a software tool for the bifurcation analysis of delay differential equations. Labels $a$, $b$, $c$, $d$ along the curve correspond to four representative periodic solutions associated with four distinct values of the coupling strength: $\lambda = \{\lambda_c, -0.4867, -0.4848, -0.4760\}$, respectively. On the right, the time series solutions $(x_1(t), x_2(t), x_3(t))$ at each of the labeled points, $a - d$, are plotted. Observe that as $\lambda$ increases away from the critical point $\lambda_c$, the amplitude of the oscillations increases as a function of the square root of the distant from the bifurcation point—a well-known characteristic feature of Hopf bifurcations.

The stability of each of the periodic solutions shown in Fig. 5(right) can be determined numerically, through calculations of Floquet multipliers, see Fig. 6. When $\lambda = -0.4871$, the dominant multiplier has magnitude exactly equal to 1, which is indicative of the bifurcation point. As $\lambda$ increases through $b$, $c$, and $d$, the amplitude of the oscillations gradually increases and, in this particular situation, the dominant multipliers all have magnitude larger than 1. Thus indicating that the Hopf bifurcation is subcritical, i.e., the emerging oscillations are unstable. Observe that all three periodic solutions, $b$, $c$, and $d$, exhibit a trivial multiplier of magnitude equal to 1. This is indeed the case because perturbations tangent to any periodic solution are neutrally stable.

The locus, in parameter space $(\lambda, \tau)$, of the branch of unstable Hopf bifurcation of Fig. 5, is now shown in Fig. 7(a). The delay-induced oscillations exist in the region just above the locus curve. The rightmost point along this two-parameter boundary curve corresponds to the condition $A = B$. The leftmost point is the Hopf bifurcation point without delay, i.e., $\tau = 0$. Substituting $\tau = 0$ in (7) we can solve for $\omega$, which then yields the condition $B = 2A$ for the Hopf bifurcation without delay. Notice that this is the same condition produced by Eq. (8). Figs. 7(b)–(d) illustrate the contraction that occurs in the basin of attraction of synchronous equilibria due to delay-induced instability.

Since the small amplitude oscillations found in Fig. 7(a) are unstable then almost all solutions beyond the Hopf point will approach the large amplitude periodic orbit, making it a global attractor. But this is good news for the coupled-core fluxgate magnetometer because

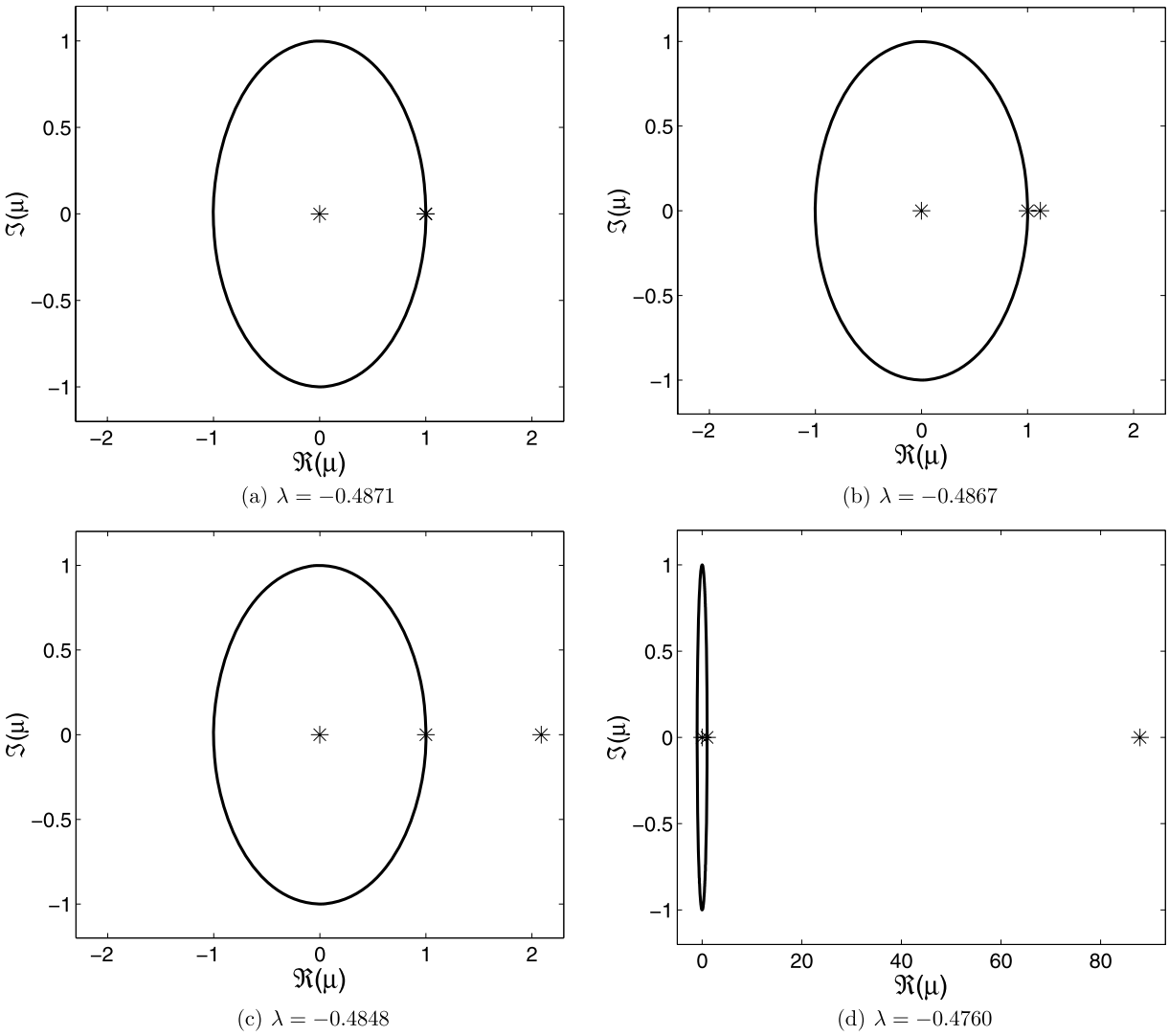


**Fig. 6.** Numerical calculations of Floquet multipliers for periodic solutions shown in Fig. 5(right). (a) Exactly at the bifurcation when $\lambda = \lambda_c$, the magnitude of the dominant multiplier is equal to 1. As $\lambda$ increases through *b*, *c*, and *d*, the magnitude of the dominant multiplier becomes larger than 1 and so the emerging oscillations are deemed to be unstable.

the net effect of the delay is essentially to increase the basin of attraction of the global branch of large-amplitude oscillations between the two magnetization states of the ferromagentic materials. In other words, delayed coupling tends to enhance the basin of attraction of the global branch of oscillations so that it becomes more robust to induce a CCFM-based device to oscillate on its own. Similar loci of unstable small-amplitude oscillations are found for arrays with larger $N$, they are now shown for brevity.

The criticality of the Hopf bifurcation can also be determined rigorously by performing a Center Manifold reduction of the original model equations (5) around the synchronous equilibrium $(y_1, \ldots, y_N) = (\bar{y}, \ldots, \bar{y})$. We perform the reduction with the aid of the software package Maple [19] using the outline given in [20] for the special case of $N = 3$ fluxgates. We list only the main results while the details of the computations can be found in Appendix A. We start by shifting the equilibrium in (5) to the origin and rewrite the resulting vector field equation in the following form

$$\mathbf{v}'(t) = \mathbf{A}_0\mathbf{v}(t) + \mathbf{A}_1\mathbf{v}(t-\tau) + \mathbf{f}\big(\mathbf{v}(t), \mathbf{v}(t-\tau)\big), \tag{9}$$

where

$$\mathbf{v}(t) = \begin{bmatrix} y_1 - \bar{y} \\ y_2 - \bar{y} \\ y_3 - \bar{y} \end{bmatrix}, \qquad \mathbf{A}_0 = \begin{bmatrix} a_{11} & a_{12} & 0 \\ 0 & a_{11} & a_{12} \\ 0 & 0 & a_{11} \end{bmatrix}, \qquad \mathbf{A}_1 = \begin{bmatrix} 0 & 0 & 0 \\ 0 & 0 & 0 \\ a_{12} & 0 & 0 \end{bmatrix},$$

$$\mathbf{f} = \begin{bmatrix} b_1\big(\frac{v_1^2}{2} + \lambda v_1 v_2 + \frac{\lambda^2}{2} v_2^2\big) + b_2\big(\frac{v_1^3}{6} + \frac{\lambda}{2} v_1^2 v_2 + \frac{\lambda^2}{2} v_1 v_2^2 + \frac{\lambda^3}{6} v_2^3\big) \\ b_1\big(\frac{v_2^2}{2} + \lambda v_2 v_3 + \frac{\lambda^2}{2} v_3^2\big) + b_2\big(\frac{v_2^3}{6} + \frac{\lambda}{2} v_2^2 v_3 + \frac{\lambda^2}{2} v_2 v_3^2 + \frac{\lambda^3}{6} v_3^3\big) \\ b_1\big(\frac{v_3^2}{2} + \lambda v_3 v_1(t-\tau) + \frac{\lambda^2}{2} v_1^2(t-\tau)\big) + b_2\big(\frac{v_3^3}{6} + \frac{\lambda}{2} v_3^2 v_1(t-\tau) + \frac{\lambda^2}{2} v_3 v_1^2(t-\tau) + \frac{\lambda^3}{6} v_1^3(t-\tau)\big) \end{bmatrix},$$

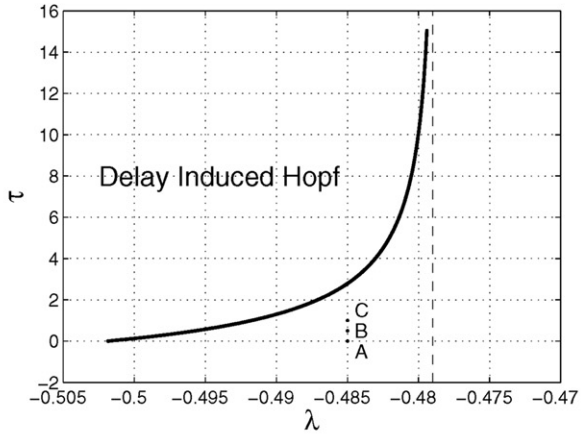


(a) Locus of delayed-induced Hopf

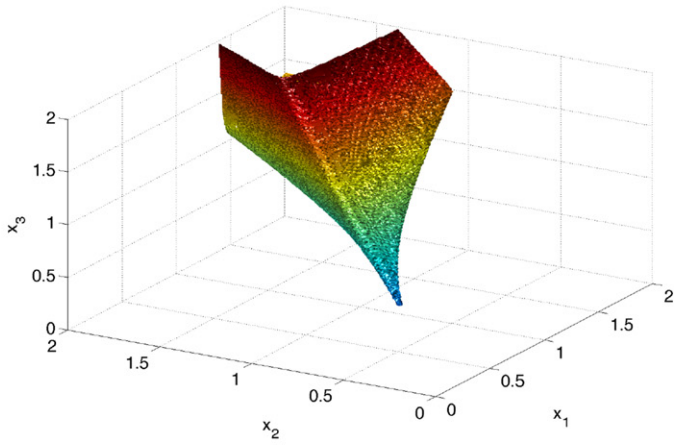


(b) A: $\tau = 0.0$

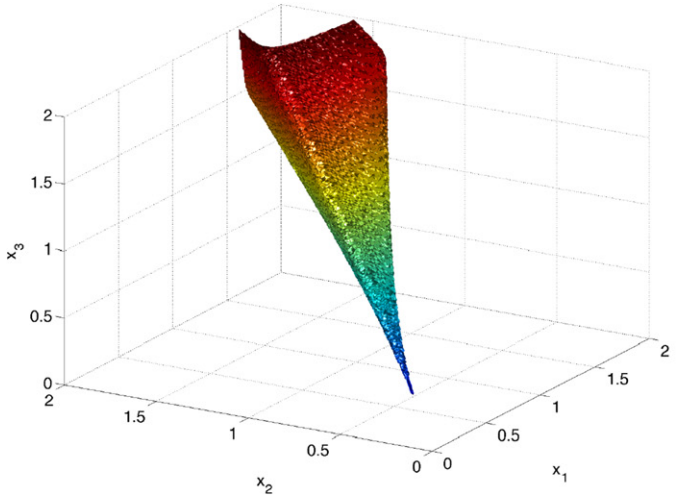


(c) B: $\tau = 0.5$

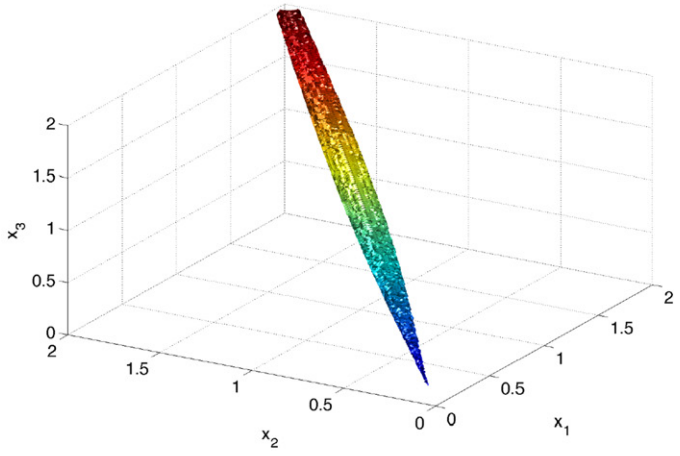


(d) C: $\tau = 1.0$

**Fig. 7.** (a) Locus of Hopf bifurcation induced by delayed coupling in a ring with $N = 3$ overdamped bistable systems governed by Eq. (4). (b)–(d) Basins of attraction of synchronous equilibria for delay values labeled A, B, and C in (a), respectively. For small $\tau$, both synchronous equilibria and large-amplitude oscillations have reasonably large basins of attraction. As $\tau$ increases towards the locus of the Hopf bifurcation, however, the equilibria lose stability, and consequently, their basins of attraction shrink accordingly.

and $a_{11} = -1 + c(1-\bar{y}^2)$, $a_{12} = c\lambda(1-\bar{y}^2)$, $b_1 = -2c^2\bar{y}(1-\bar{y}^2)$, $b_2 = 2(1-\bar{y}^2)(3\bar{y}^2-1)$. The linearization of (9) about the trivial solution is

$$\mathbf{v}'(t) = \mathbf{A}_0\mathbf{v}(t) + \mathbf{A}_1\mathbf{v}(t-\tau). \tag{10}$$

Since the solution space for Eqs. (9) and (10) is infinite dimensional, it is common practice to define the phase-point at time $t$ through

$$\mathbf{v}_t(\theta) = \mathbf{v}(t+\theta), \quad -\tau \leqslant \theta \leqslant 0.$$

Then the phase-space is $\mathcal{C} = C([-\tau, 0], R^3)$, i.e., the space of continuous functions mapping the interval $[-\tau, 0]$ into $R^3$. We then seek a decomposition of the solution space for (10) as

$$\mathcal{C} = E \oplus S,$$

where $E$ is an $m$-dimensional invariant subspace spanned by the solutions to (10) corresponding to the eigenvalues with zero real part. $S$ is infinite dimensional and an invariant subspace corresponding to the eigenvalues with nonzero (usually negative) real part.

At the critical delay $\tau_c$ where a Hopf bifurcation occurs, the trivial solution of (9) has an $m = 2$ dimensional center eigenspace, $E$, with basis

$$\Phi(\theta) = \big[\phi_1(\theta) \,\big|\, \phi_2(\theta)\big], \qquad \phi_1 = \begin{bmatrix} a_{12}\cos\omega\theta \\ a_{11}\cos\omega\theta + \omega\sin\omega\theta \\ \frac{(a_{11}^2-\omega^2)}{a_{12}}\cos\omega\theta - \frac{2\omega a_{11}}{a_{12}}\sin\omega\theta \end{bmatrix}, \qquad \phi_2 = \begin{bmatrix} -a_{12}\sin\omega\theta \\ a_{11}\sin\omega\theta - \omega\cos\omega\theta \\ \frac{(a_{11}^2-\omega^2)}{a_{12}}\sin\omega\theta + \frac{2\omega a_{11}}{a_{12}}\cos\omega\theta \end{bmatrix} \tag{11}$$

and an infinite dimensional stable eigenspace $S$. The corresponding Center Manifold is given by

$$M_f = \{\phi \in C \mid \phi = \Phi\mathbf{u} + \mathbf{h}(\mathbf{u})\},$$

where $\mathbf{u} = [u_1, u_2]^T$ are coordinates on $E$ and $\mathbf{h}(\mathbf{u}) \in S$. Solutions to (10) on $M_f$ are given by $\mathbf{v}_t = \Phi(\theta)\mathbf{u}(t) + \mathbf{h}(\theta, \mathbf{u})$, which can be rewritten as

$$\mathbf{v}_t(\theta) = \begin{bmatrix} (a_{12}\cos\omega\theta)u_1 - (a_{12}\sin\omega\theta)u_2 \\ (a_{11}\cos\omega\theta + \omega\sin\omega\theta)u_1 + (a_{11}\sin\omega\theta - \omega\cos\omega\theta)u_2 \\ \left(\frac{(a_{11}^2-\omega^2)}{a_{12}}\cos\omega\theta - \frac{2\omega a_{11}}{a_{12}}\sin\omega\theta\right)u_1 + \left(\frac{(a_{11}^2-\omega^2)}{a_{12}}\sin\omega\theta + \frac{2\omega a_{11}}{a_{12}}\cos\omega\theta\right)u_2 \end{bmatrix} + \begin{bmatrix} h_{11}^1(\theta)u_1^2 + h_{12}^1(\theta)u_1u_2 + h_{22}^1(\theta)u_2^2 \\ h_{11}^2(\theta)u_1^2 + h_{12}^2(\theta)u_1u_2 + h_{22}^2(\theta)u_2^2 \\ h_{11}^3(\theta)u_1^2 + h_{12}^3(\theta)u_1u_2 + h_{22}^3(\theta)u_2^2 \end{bmatrix} + O\left(\|\mathbf{u}\|^3\right).$$

The $h_{jk}^i(\theta)$ terms are found by solving an ODE boundary value problem, see Appendix A for details. The dynamics on the Center Manifold reduces, up to $O(\|\mathbf{u}\|^4)$, to the following system of ODEs

$$\begin{aligned} \dot{u}_1 &= \omega u_2 + \Psi_{12}(0)\left(f_{11}u_1^2 + f_{12}u_1u_2 + f_{22}u_2^2 + f_{111}u_1^3 + f_{112}u_1^2u_2 + f_{122}u_1u_2^2 + f_{222}u_2^3\right), \\ \dot{u}_2 &= -\omega u_1 + \Psi_{22}(0)\left(f_{11}u_1^2 + f_{12}u_1u_2 + f_{22}u_2^2 f_{111}u_1^3 + f_{112}u_1^2u_2 + f_{122}u_1u_2^2 + f_{222}u_2^3\right) \end{aligned} \tag{12}$$

where $\Psi(\xi)$ is a basis for the solutions of the adjoint equation for (10), see Appendix A for details. The coefficients $f_{jk}$ and $f_{ijk}$ are functions of the parameters that control the CCFM, i.e., $c$, $\lambda$, and $\varepsilon$, the Hopf frequency $\omega$, and the Center Manifold coefficients $h_{jk}^i(0)$ and $h_{jk}^i(-\tau)$.

Guckenheimer and Holmes [21] show that the critically of the Hopf bifurcation can be determined directly from the Center Manifold equations (12) through the sign of the following quantity

$$\begin{aligned} a = {} & \frac{1}{8}\left[\Psi_{12}(0)(3f_{111} + f_{122}) + \Psi_{22}(0)(f_{112} + 3f_{222})\right] \\ & - \frac{1}{8\omega}\left[\left(\Psi_{12}(0)^2 - \Psi_{22}(0)^2\right)f_{12}(f_{11} + f_{22}) + 2\Psi_{12}(0)\Psi_{22}(0)\left(f_{22}^2 - f_{11}^2\right)\right]. \end{aligned} \tag{13}$$

If $a < 0$ the Hopf bifurcation is supercritical and if $a > 0$ it is subcritical. An analytical expression for $a$ for the CCFM device (with $N = 3$) was derived with the aid of Maple but it was excessively large for further analytical results. A numerical value can be calculated, however, for a particular set of parameter values. For instance, direct calculations via Maple show that when $c = 3$, $\varepsilon = 0$, $\tau = 2.0$, and $\lambda = -0.487$, Eq. (13) yields the numeric value $a = 23.699457$. This result confirms that indeed the branch of Hopf bifurcations shown in Figs. 5 and 7(a) is subcritical. Details of the calculations can be found in Appendix A.

### 4.3. Performance comparison

The residence times difference (RTD), i.e., the difference in the times spent by the system in its two stable magnetization states, can be computed as

$$\Delta t \approx \frac{\pi}{\sqrt{cx_{inf}}}\left(\frac{1}{\sqrt{\lambda_c - \lambda}} - \frac{1}{\sqrt{\lambda_c - \lambda + 2\varepsilon}}\right) \tag{14}$$

which vanishes (as expected) for $\varepsilon = 0$, and can be used as a quantifier of the target signal, analogous to the time-domain operation of the single fluxgate [22]. The system responsivity (or sensitivity) is defined via the derivative $\partial\Delta t/\partial\varepsilon$. In the absence of delay, we have shown, theoretically and experimentally [5], that sensitivity increases dramatically as one approaches the critical point in the oscillatory regime. This result suggests that careful tuning of the coupling parameter so that the oscillations have very low frequency, could offer significant benefits for the detection of very small target signals. Coupling, therefore, allows one to exploit the target-signal dependence of the emergent oscillations for detection and quantification purposes.

Since $\Delta t$ is independent of the period of the oscillations, it follows that in the absence of delay the sensitivity of the device should remain unchanged, provided that the strength of the external signal $\varepsilon$ has no changed. This claim is confirmed, numerically, in Fig. 8. As expected, the period of the oscillations increases, see Fig. 8(left), as the delay increases. However, the RTD response remains unchanged as is shown in Fig. 8(right).

Changing $\varepsilon$, however, has the effect of changing the asymmetry in the oscillating wave form, and so they RTD response should change accordingly, as is illustrated in Fig. 9.

## 5. Discussion

In this manuscript, we have expanded our earlier work on coupled overdamped bistable systems to investigate the effects of delayed coupling on synchronous equilibrium points and on collective oscillations that emerge from a global branch of heteroclinic connections between different saddle-node equilibria. These oscillations have shown to be excellent detectors of small external dc and ac signals because the long period, which occurs near the onset of the heteroclinic connection, renders their wave form highly sensitive to symmetry-breaking effects caused by very small signals. This critical observation has led to the fabrication of highly-sensitive sensors, magnetic- and electric-field ones, whose operation relies mainly on the coupling signal that travels from one bistable system to the next one. While special care has been placed to use high-speed components in the coupling circuit, in practice we must still account for small delays.

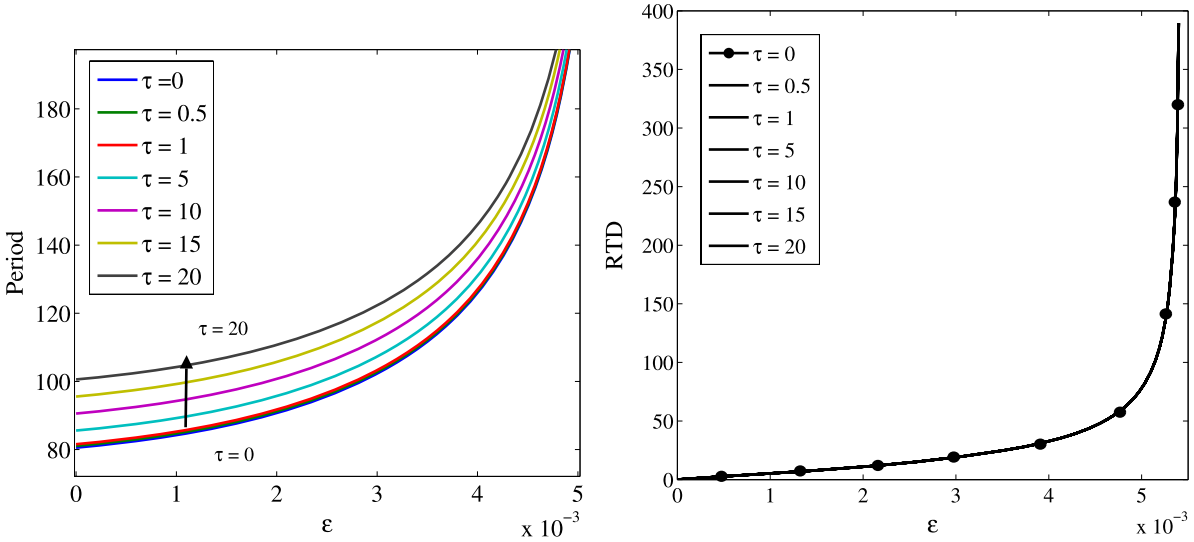


**Fig. 8.** Sensitivity response of a CCFM under the presence of delay. (Left) Period of the oscillations increases as the interaction delay increases. (Right) However, the sensitivity response, as measured by the RTD curve remains the same.

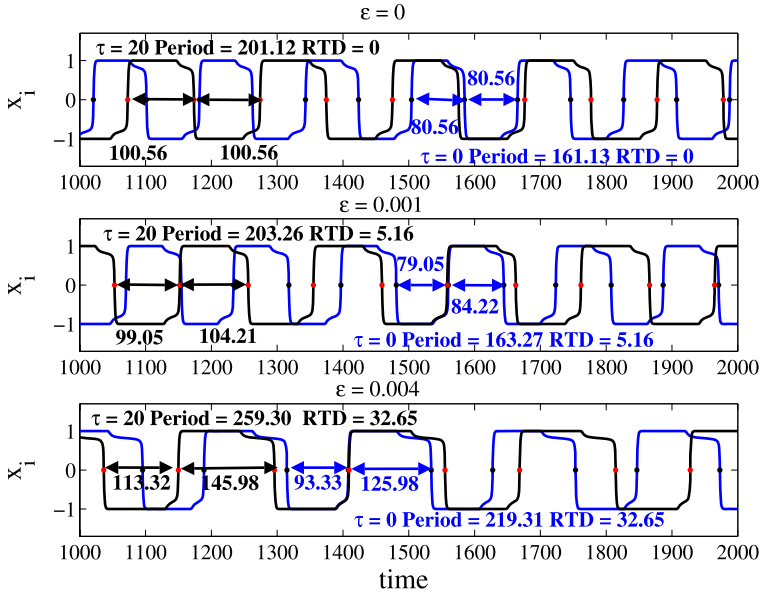


**Fig. 9.** Changes in the strength of an incoming signal, while the delay is held constant, alter the asymmetry of the large-amplitude oscillations which in turn lead to changes in the RTD readout.

Thus, we have investigated its effects on equilibrium points and oscillations of the coupled bistable system. In particular, we have focused this work to study the region close to the onset of oscillations where, in the absence of delay, both the synchronous equilibria and oscillations are stable, and in which the coupled sensor device yields its maximum performance in terms of sensitivity. When delays are introduced into the system, the negative feedback system is destabilized, which has often been observed [23,16,17]. Analysis of the governing equations combined with our numerical results shows that a delay-induced Hopf bifurcation results in almost all solutions tending to a globally attracting large amplitude oscillation. However, even small delays (sub-Hopf) in the system cause reduced stability of the synchronous equilibrium, which substantially reduces its basin of attraction. From a design perspective it would be valuable to measure the delays to gain insight into the increased region for operational sensitivity of the CCFM. Techniques have been developed to estimate delays of delay differential equations, where the delay has a strong effect on the dynamics of the solution [25,26,24]. However, our model shows that the delays primarily affect the basin of attraction for the symmetric equilibrium, which undergoes a subcritical Hopf bifurcation and then the solution jumps to the stable heteroclinic periodic solution, which is minimally dependent on the delay. Thus, parameter estimation methods for the delays from experimental measurements compared to the model are unlikely to obtain good estimates of the actual delays in the system. Under the conditions of operation of the coupled sensor device, the delay-induced oscillations in the bistable dynamics are generically unstable so the net effect of delayed coupling is to increase the basin of attraction of the global branch of periodic oscillations. But this is a positive effect since the sensor device depends mainly on large amplitude oscillatory behavior. Consequently, a small delay can facilitate the coupled sensor device to oscillate on its own for a greater number of initial conditions.

**Acknowledgements**

We gratefully acknowledge support from the Office of Naval Research (Code 331) and SPAWAR internal S&T program. A.P. and D.L. were supported in part by National Science Foundation grants CMS-0625427 and CMMI-0923803, and by DoD – SPAWAR Command grant N66001-08-D-0154.

## Appendix A. Center Manifold reduction

In this Appendix, we provide a self-contained review of the Center Manifold reduction relevant to this work. In particular, we illustrate the process of reducing the dynamics of a CCFM device subject to delay for the special case of $N = 3$ fluxgates. Since the computations are too large to be carried out manually (and also to print them out), we include a Maple program that automates the reduction process. An extension of the reduction process, and the Maple code, for larger arrays is straightforward.

Consider again the model equations of a CCFM device with $N = 3$ fluxgates

$$\mathbf{v}'(t) = \mathbf{A}_0\mathbf{v}(t) + \mathbf{A}_1\mathbf{v}(t-\tau) + \mathbf{f}\big(\mathbf{v}(t), \mathbf{v}(t-\tau)\big), \tag{A.1}$$

defined over $\mathcal{C} = C([-\tau, 0], R^3)$ which is the space of continuous functions mapping the interval $[-\tau, 0]$ into $R^3$. $\mathbf{A}_0$, $\mathbf{A}_1$, and $\mathbf{f}$ are as defined in Eq. (9) of Section 4. We recall that (A.1) admits the trivial solution $(v_1, v_2, v_3) = (0, 0, 0)$, which corresponds to the synchronous equilibrium $(y_1, y_2, y_3) = (\bar{y}, \bar{y}, \bar{y})$ of the original model equations (5). The stability properties of the trivial solution can be studied through the linearized system

$$\mathbf{v}'(t) = L(\mathbf{v}_t), \tag{A.2}$$

where

$$\mathbf{v}_t(\theta) = \mathbf{v}(t+\theta), \quad -\tau \leqslant \theta \leqslant 0$$

is the phase-point at time $t$ and the linear map $L : \mathcal{C} \times R^3 \to R^3$ is defined by

$$L\big(\phi(\theta)\big) = \begin{bmatrix} a_{11} & a_{12} & 0 \\ 0 & a_{11} & a_{12} \\ 0 & 0 & a_{11} \end{bmatrix} \begin{bmatrix} \phi_1(0) \\ \phi_2(0) \\ \phi_3(0) \end{bmatrix} + \begin{bmatrix} 0 & 0 & 0 \\ 0 & 0 & 0 \\ a_{12} & 0 & 0 \end{bmatrix} \begin{bmatrix} \phi_1(-\tau) \\ \phi_2(-\tau) \\ \phi_3(-\tau) \end{bmatrix}.$$

Notice that (A.2) in DDE form corresponds to $\mathbf{v}'(t) = \mathbf{A}_0\mathbf{v}(t) + \mathbf{A}_1\mathbf{v}(t-\tau)$. The characteristic equation of this linearized system can be written as

$$\Delta(\sigma) = 0, \quad \text{where} \quad \Delta(\sigma) = \sigma - Le^{\sigma}.$$

The infinitesimal generator of the semigroup defined by Eq. (A.2) has eigenvalues $\{\pm\omega i\}$ and the corresponding eigenspaces are given by the nullspaces of $\pm\omega i I$. Let $\phi_i(\theta) = [\phi_{i1}, \phi_{i2}, \phi_{i3}]^T$, for $i = 1, 2$. For the eigenvalue $\omega i$ we must solve

$$(\omega i I - L)\phi_1 = \omega i \phi_1 - \dot{\phi}_1 = 0,$$

which yields $\phi_1(\theta) = [ae^{\omega\theta i}, be^{\omega\theta i}, ce^{\omega\theta i}]^T$, where $a$, $b$, and $c$ are arbitrary constants. These constants can be found by considering the initial condition $\dot{\phi}_1(0) = L(\phi(\theta))$, so that

$$\begin{bmatrix} \omega i - a_{11} & -a_{12} & 0 \\ 0 & \omega i - a_{11} & -a_{12} \\ -a_{12}e^{\omega\tau i} & 0 & \omega i - a_{11} \end{bmatrix} \begin{pmatrix} a \\ b \\ c \end{pmatrix} = \begin{bmatrix} 0 \\ 0 \\ 0 \end{bmatrix}.$$

Since the matrix has determinant zero, we let $a = -a_{12}$ so that $b = a_{11} - \omega i$, and $c = (\omega i - a_{12})^2/a_{12}$.

We now seek a decomposition of the solution space for (A.2) as

$$\mathcal{C} = E \oplus S,$$

where $E$ is an $m$-dimensional invariant subspace spanned by the solutions to (A.2) corresponding to the eigenvalues with zero real parts. And $S$ is an infinite dimensional invariant subspace associated with nonzero eigenvalues (typically negative eigenvalues). In the case of a CCFM device with $N = 3$ fluxgates, $m = 2$ and the basis for the center eigenspace $E$ is then given by $\Phi(\theta) = [Re\{\phi_1(\theta)\} \mid Im\{\phi_1(\theta)\}]$ which we write explicitly

$$\Phi(\theta) = \begin{bmatrix} a_{12}\cos\omega\theta & -a_{12}\sin\omega\theta \\ a_{11}\cos\omega\theta + \omega\sin\omega\theta & a_{11}\sin\omega\theta - \omega\cos\omega\theta \\ \frac{(a_{11}^2-\omega^2)}{a_{12}}\cos\omega\theta - \frac{2\omega a_{11}}{a_{12}}\sin\omega\theta & \frac{(a_{11}^2-\omega^2)}{a_{12}}\sin\omega\theta + \frac{2\omega a_{11}}{a_{12}}\cos\omega\theta \end{bmatrix}.$$

The Center Manifold theorem then guarantees that there is an $m$-dimensional manifold of (A.1) given by

$$M_f = \big\{\phi \in \mathcal{C} \mid \phi = \Phi\mathbf{u} + \mathbf{h}(\mathbf{u})\big\},$$

where $\mathbf{h}(\mathbf{u}) \in S$ and $\mathbf{u}(t) \in R^m$. The flow on the Center Manifold is given by

$$\mathbf{v}_t(\theta) = \Phi(\theta)\mathbf{u}(t) + \mathbf{h}\big(\theta, \mathbf{u}(t)\big),$$

where $\mathbf{u}(t) = [u_1(t), u_2(t)]^T$ is a solution of the dynamics restricted to the Center Manifold as is governed by the following system of ODEs:

$$\dot{\mathbf{u}} = B\mathbf{u} + \Psi(0) f\big(\Phi\mathbf{u} + \mathbf{h}(\mathbf{u})\big). \tag{A.3}$$

$B$, $\Psi$ and $\mathbf{h}$ are as defined below:

$$B = \begin{bmatrix} 0 & \omega \\ -\omega & 0 \end{bmatrix}, \qquad \Psi(s) = \begin{bmatrix} \psi_{11}(s) & \psi_{12}(s) & \psi_{13}(s) \\ \psi_{21}(s) & \psi_{22}(s) & \psi_{23}(s) \end{bmatrix}, \qquad \mathbf{h} = \begin{bmatrix} h^1_{11}(\theta)u_1^2 + h^1_{12}(\theta)u_1u_2 + h^1_{22}(\theta)u_2^2 \\ h^2_{11}(\theta)u_1^2 + h^2_{12}(\theta)u_1u_2 + h^2_{22}(\theta)u_2^2 \\ h^3_{11}(\theta)u_1^2 + h^3_{12}(\theta)u_1u_2 + h^3_{22}(\theta)u_2^2 \end{bmatrix} + O\big(\|\mathbf{u}\|^3\big).$$

$\Psi$, in particular, is a basis for the *transposed* or (adjoint) system $\mathbf{z}'(t) = L^T(\mathbf{z}_t)$, where

$$L^T(\psi) = -\psi(0)\mathbf{A}_0 - \psi(\tau)\mathbf{A}_1.$$

The eigenvalues of $L^T$ are also $\{\pm\omega i\}$, so the computation of $\Psi$ mimics that of $\Phi$ but with the adjoint linear operator $L^T$. Furthermore, if we also require that $\langle\Psi, \Phi\rangle = I$ then any solution $\mathbf{u} \in R^m$ on the Center Manifold can be obtained by a direct projection $\mathbf{u} = \langle\Psi, \xi\rangle$, where $\xi = \Phi\mathbf{u} \in E$. The inner product operation is defined as follows

$$\langle\psi_j, \phi_k\rangle = \psi_j(0)\cdot\phi_k(0) + \int_{-\tau}^{0} \Psi_j(\theta+\tau)A_1\phi_k(\theta)\,d\theta.$$

In our case, this operation simplifies to

$$\langle\psi_j, \phi_k\rangle = \psi_j(0)\cdot\phi_k(0) + a_{12}\int_{-\tau}^{0} \Psi_{j3}(\theta+\tau)\phi_{k1}(\theta)\,d\theta.$$

Direct calculations yield the desired basis $\Psi(s)$, but is expression is too complex and long for further analysis. Finally, the vector $\mathbf{h}(\mathbf{u})$ is found by solving the following system of PDEs:

$$\frac{\partial\mathbf{h}}{\partial\mathbf{u}}\big\{B\mathbf{u} + \Psi(0)f\big[\Phi(\theta)\mathbf{u} + \mathbf{h}(\theta,\mathbf{u})\big]\big\} + \Phi(\theta)\Psi(0)f\big[\Phi(\theta)\mathbf{u} + \mathbf{h}(\theta,\mathbf{u})\big]$$
$$= \begin{cases} \frac{\partial\mathbf{h}}{\partial\theta}, & -\tau \leqslant \theta < 0, \\ L(\mathbf{h}(\theta,\mathbf{u})) + f[\Phi(\theta)\mathbf{u} + \mathbf{h}(\theta,\mathbf{u})], & \theta = 0. \end{cases}$$

Now that the reduction is complete, the criticality of the Hopf bifurcation can be determined from the reduced equations (A.3). The entire reduction process was automated with the aid of Maple. Table A.1 shows the actual code.

**Table A.1**
Maple code for a Center Manifold reduction of a CCFM device with $N = 3$ fluxgates subject to delay.

```
# Usage: read cm-reduction
# —— Define Characteristic Matrix Equation ——
with(LinearAlgebra):
A0 := Matrix(3,[[a11,a12,0],[0,a11,a12],[0,0,a11]]);
A1 := Matrix(3,[[0,0,0],[0,0,0],[a12,0,0]]);
ident := Matrix(3,[[1,0,0],[0,1,0],[0,0,1]]):
Delta := lambda*ident-A0-exp(-lambda*tau)*A1;
chareq := Determinant(Delta);
# —— Find Basis Φ(θ) for Center Eigenspace E ——
v := Matrix([[v1], [v2], [v3]]);
Dv := subs(lambda = I*omega, Delta.v);
v1 := -a12;
v2 := solve(Dv[1, 1], v2);
v3 := solve(Dv[2, 1], v3);
yy := map(evalc, exp(I*omega*theta)*v);
Phi := Matrix([[coeff(yy[1, 1], I, 0), coeff(yy[1, 1], I, 1)], [coeff(yy[2, 1], I, 0), coeff(yy[2, 1], I,1)], [coeff(yy[3, 1], I, 0), coeff(yy[3, 1], I, 1)]]);
# —— Find Adjoint Basis Ψ(s) for Center Eigenspace E ——
u := Matrix([[u1], [u2]]);
Phiu := Phi.u;
B := Matrix([[0, omega], [-omega, 0]]);
w := Matrix([w1, w2, w3]);
wD := subs(lambda = I*omega, w.Delta);
w3 := -a12;
w2 := solve(wD[1, 3], w2);
w1res := w[1] = solve(wD[1, 2], w1);
yy := map(evalc, subs(lambda = I*omega, w*exp(-I*xi)));
```

**Table A.1** (*Continued*)

```
Psig := Matrix([[coeff(yy[1, 1], I, 0), coeff(yy[1, 2], I, 0), coeff(yy[1, 3], I, 0)], [coeff(yy[1, 1], I, 1), coeff(yy[1, 2], I, 1), coeff(yy[1, 3], I, 1)]]);
produit := Matrix(2, 2):
for I1 to 2 do
for I2 to 2 do
rowvec := Row(Psig, I1);
colvec := Column(Phi, I2);
produit[I1, I2] := eval(bilinearform(rowvec, colvec));
end do;
end do;
K := MatrixInverse(produit):
PPsi := map(simplify, K.Psig):
Psi0 := map(simplify, map(eval, subs(xi = 0, evalm(PPsi)))):
# —— Define Coordinates on Center Manifold ——
h := Matrix([[h1_11(theta) * u1^2 + h1_12(theta) * u1 * u2 + h1_22(theta) * u2^2], [h2_11(theta) * u1^2 + h2_12(theta) * u1 * u2 + h2_22(theta) * u2^2],
[h3_11(theta) * u1^2 + h3_12(theta) * u1 * u2 + h3_22(theta) * u2^2]]);
x := Matrix([[x1], [x2], [x3]]);
xt := Matrix([[x1t], [x2t], [x3t]]);
lin := A0.x+A1.xt;
f1 := -2 * c^2 * xe * γ * ((1/2) * x1^2 + κ * x1 * x2 + (1/2) * κ^2 * x2^2) + 2 * c^3 * γ * (2 - 3 * γ) * ((1/6) * x1^3 + (1/2) * κ * x1^2 * x2
+ (1/2) * kappa * x1 * x2^2 + (1/6) * κ^3 * x2^3);
f2 := -2 * c^2 * xe * γ * ((1/2) * x2^2 + κ * x2 * x3 + (1/2) * κ^2 * x3^2) + 2 * c^3 * γ * (2 - 3 * γ) * ((1/6) * x2^3 + (1/2) * κ * x2^2 * x3
+ (1/2) * κ * x2 * x3^2 + (1/6) * κ^3 * x3^3);
f3 := -2 * c^2 * xe * γ * ((1/2) * x3^2 + κ * x3 * x1t + (1/2) * κ^2 * x1t^2) + 2 * c^3 * γ * (2 - 3 * γ) * ((1/6) * x3^3 + (1/2) * κ * x3^2 * x1t
+ (1/2) * κ * x3 * x1t^2 + (1/6) * κ^3 * x1t^3);
f := Matrix([[f1], [f2], [f3]]):
nlin := Matrix([[f1], [f2], [f3]]);
Phiu0 := map(eval, subs(theta = 0, Phiu));
Phiut := map(eval, subs(theta = -tau, Phiu));
xce := [x1 = Phiu0[1, 1], x2 = Phiu0[2, 1], x3 = Phiu0[3, 1],
x1t = Phiut[1, 1], x2t = Phiut[2, 1], x3t = Phiut[3, 1]];
Phiuh0 := map(eval, subs(theta = 0, Phiu+h));
Phiuht := map(eval, subs(theta = -tau, Phiu+h));
xcm := [x1 = Phiuh0[1, 1], x2 = Phiuh0[2, 1], x3 = Phiuh0[3, 1],
x1t = Phiuht[1, 1], x2t = Phiuht[2, 1], x3t = Phiuht[3, 1]];
# —— Define ODEs for h Function ——
delhs := map(diff, h, theta);
dhdu := Matrix([[diff(h[1, 1], u1), diff(h[1, 1], u2)], [diff(h[2, 1], u1), diff(h[2, 1],u2)], [diff(h[3, 1], u1), diff(h[3, 1], u2)]]);
derhs := map(collect, map(expand, dhdu.B.u+Phi.Psi0.subs(xce, f)), [u1, u2, u3], distributed, factor):
hdes := delhs-derhs:
de1 := coeff(coeff(hdes[1, 1], u1^2), u2, 0); de2 := coeff(coeff(hdes[1, 1], u1), u2) :
de3 := coeff(coeff(hdes[1, 1], u2^2), u1, 0) : de4 := coeff(coeff(hdes[2, 1], u1^2), u2, 0) :
de5 := coeff(coeff(hdes[2, 1], u1), u2) : de6 := coeff(coeff(hdes[2, 1], u2^2), u1, 0) :
de7 := coeff(coeff(hdes[3, 1], u1^2), u2, 0) : de8 := coeff(coeff(hdes[3, 1], u1), u2) :
de9 := coeff(coeff(hdes[3, 1], u2^2), u1, 0) :
des := {de1, de2, de3, de4, de5, de6, de7, de8, de9} :
fns :=
{coeff(h[1, 1], u1^2), coeff(h[1, 1], u2^2), coeff(h[2, 1], u1^2), coeff(h[2, 1], u2^2), coeff(h[3, 1], u1^2), coeff(h[3, 1], u2^2), coeff(coeff(h[1, 1], u1), u2),
coeff(coeff(h[2, 1], u1), u2), coeff(coeff(h[3, 1], u1), u2)};
temp := dsolve(des, fns):
changeC := [C1 = C1, C2 = C2, C3 = C3, C4 = C4, C5 = C5, C6 = C6, C7 = C7, C8 = C8, C9 = C9];
hsoln := simplify(expand(evalc(subs(changeC, value(temp))))):
collect(hsoln[9], [Psi11(0), Psi12(0), Psi13(0), Psi21(0), Psi22(0), Psi23(0)], factor);
hsoln0 := simplify(eval(subs(theta = 0, hsoln))):
hsolnt := simplify(eval(subs(theta = -tau, hsoln))):
bclhs := map(eval, subs(theta = 0, derhs)):
bcrhs := map(collect, subs(xcm, lin)+subs(xce, nlin), [u1, u2]):
consts := [C1, C2, C3, C4, C5, C6, C7, C8, C9];
bceq := subs(hsoln0, hsolnt, bclhs-bcrhs):
bc1 := collect(coeff(coeff(bceq[1, 1], u1, 2), u2, 0), consts):
bc2 := collect(coeff(coeff(bceq[1, 1], u1, 1), u2, 1), consts):
bc3 := collect(coeff(coeff(bceq[1, 1], u1, 0), u2, 2), consts):
bc4 := collect(coeff(coeff(bceq[2, 1], u1, 2), u2, 0), consts):
bc5 := collect(coeff(coeff(bceq[2, 1], u1, 1), u2, 1), consts):
bc6 := collect(coeff(coeff(bceq[2, 1], u1, 0), u2, 2), consts):
bc7 := collect(coeff(coeff(bceq[3, 1], u1, 2), u2, 0), consts):
bc8 := collect(coeff(coeff(bceq[3, 1], u1, 1), u2, 1), consts):
bc9 := collect(coeff(coeff(bceq[3, 1], u1, 0), u2, 2), consts):
bcs := {bc1, bc2, bc3, bc4, bc5, bc6, bc7, bc8, bc9} :
consts := convert(consts, set);
Csoln := map(simplify, solve(bcs, consts)):
collect(Csoln[2], [Psi0[1, 1], Psi0[1, 2], Psi0[1, 3], Psi0[2, 1], Psi0[2, 2], Psi0[2, 3]], factor);
# —— Calculate Nonlinear Terms ——
fu := collect(expand(subs(xcm, f)), [u1, u2, u3], distributed, factor):
nonlinu := Matrix([fu]):
nonlinODE := Psi0.nonlinu:
```

(*continued on next page*)

**Table A.1** (*Continued*)

```
# —— Calculate Criticality Coefficient a ——
quad[1, 1] := coeff(coeff(nonlinODE[1, 1], u1, 2), u2, 0);
quad[1, 2] := coeff(coeff(nonlinODE[1, 1], u1, 1), u2, 1);
quad[1, 3] := coeff(coeff(nonlinODE[1, 1], u1, 0), u2, 2);
quad[2, 1] := coeff(coeff(nonlinODE[2, 1], u1, 2), u2, 0);
quad[2, 2] := coeff(coeff(nonlinODE[2, 1], u1, 1), u2, 1);
quad[2, 3] := coeff(coeff(nonlinODE[2, 1], u1, 0), u2, 2);
cub[1, 1] := coeff(coeff(nonlinODE[1, 1], u1, 3), u2, 0);
cub[1, 3] := coeff(coeff(nonlinODE[1, 1], u1, 1), u2, 2);
cub[2, 2] := coeff(coeff(nonlinODE[2, 1], u1, 2), u2, 1);
cub[2, 4] := coeff(coeff(nonlinODE[2, 1], u1, 0), u2, 3);
atmp := collect(simplify(1/8*(3*cub[1, 1]+cub[1, 3] + cub[2, 2]+3*cub[2, 4])-(quad[1,2]*(quad[1, 1]+ quad[1, 3])-quad[2, 2]*(quad[2, 1]
+quad[2, 3])-2*quad[1, 1]*quad[2, 1] + 2*quad[1, 3]*quad[2, 3])/(8*omega)), [Psi0[1, 2], Psi0[2, 2]], distributed, factor);
a := subs(Psi0,simplify(subs(Csoln,simplify(subs(subs(hsoln0,hsolnt,atmp)))));
# —— Bilinear Operation ——
bilinearform := proc (rowv, colv)
local pstemp;
pstemp := subs(xi = 0, theta = 0, BilinearForm(rowv, colv, conjugate = false))
+int(subs(xi = sigma+tau, theta = sigma, BilinearForm(rowv, colv, A1, conjugate = false)),
sigma = -tau .. 0);
RETURN(pstemp)
end proc;
```

## References


[1] F. Primdahl, Fluxgate magnetometers, in: Bibliography of Fluxgate Magnetometers, in: Publications of the Earth Physics Branch, vol. 41, 1970.
[2] P. Ripka, Sensors Actuators A 33 (1996) 129.
[3] P. Ripka, J. Magn. Magn. Mat. 215–216 (2000) 735.
[4] V. In, A. Bulsara, A. Palacios, P. Longhini, A. Kho, J. Neff, Phys. Rev. E 68 (2003) 045102(R);
A. Bulsara, V. In, A. Kho, P. Longhini, A. Palacios, W.-J. Rappel, J. Acebron, S. Baglio, B. Ando, Phys. Rev. E 70 (2004) 036103.
[5] A. Bulsara, V. In, A. Kho, A. Palacios, P. Longhini, S. Baglio, B. Ando, Measurement Sci. Technol. 19 (2008) 075203.
[6] V. In, A. Palacios, A. Bulsara, P. Longhini, A. Kho, J. Neff, S. Baglio, B. Ando, Phys. Rev. E 73 (2006) 066121.
[7] A. Palacios, J. Aven, P. Longhini, V. In, A. Bulsara, Phys. Rev. E 74 (2006) 021122.
[8] A. Bulsara, V. In, A. Kho, A. Palacios, P. Longhini, S. Baglio, B. Ando, Measurement Sci. Technol. 19 (2008) 075203.
[9] See e.g. W. Bornhofft, G. Trenkler, in: W. Gopel, J. Hesse, J. Zemel (Eds.), Sensors, A Comprehensive Survey, vol. 5, VCH, New York, 1989;
P. Ripka, Magnetic Sensors and Magnetometers, Artech House, Boston, 2001, for good reviews.
[10] D. Gordon, R. Brown, IEEE Trans. Magn. MAG-8 (1972) 76;
C. Russell, R. Elphic, J. Slavin, Science 203 (1979) 745;
J. Lenz, IEEE Proc. 78 (1990) 973;
R. Snare, J. Means, IEEE Trans. Magn. MAG-13 (1997) 1107.
[11] R. Koch, J. Deak, G. Grinstein, Appl. Phys. Lett. 75 (1999) 3862;
M. Karlsson, J. Robinson, L. Gammaitoni, A. Bulsara, in: Proceedings of the Meeting on Marine Electromagnetics (MARELEC), Stockholm, Sweden, 2001.
[12] F. Primdahl, J. Phys. E 12 (1979) 241;
P. Ripka, Sensors Actuators A 33 (1992) 129;
P. Ripka, Sensors Actuators A 106 (2003) 8.
[13] A. Bulsara, C. Seberino, L. Gammaitoni, M. Karlsson, B. Lundqvist, J.W.C. Robinson, Phys. Rev. E 67 (2003) 016120.
[14] V. In, A. Bulsara, A. Palacios, P. Longhini, A. Kho, Phys. Rev. E 72 (3) (2005) 036701.
[15] E. Doedel, X. Wang, Auto94: Software for Continuation and Bifurcation Problems in Ordinary Differential Equations, Applied Mathematics Report, California Institute of Technology, July 1994.
[16] J.M. Mahaffy, J. Math. Anal. Appl. 74 (1980) 72.
[17] J.M. Mahaffy, Quart. Appl. Math. 40 (1982) 193.
[18] K. Engelborghs, T. Luzyanina, G. Samaey, D. Roose, K. Verheyden, DDE-BIFTOOL v.2.03: MATLAB package for bifurcation analysis of delay differential equations, Belgium, 2007.
[19] Waterloo Maple Software, Maple 13, University of Waterloo, Waterloo, Canada, 2001.
[20] S.A. Campbell, Calculating centre manifolds for delay differential equations using Maple, in: B. Balachandran, T. Kalmär-Nagy, D. Gilsinn (Eds.), in: Delay Differential Equations: Recent Advances and New Directions, Springer-Verlag, New York, 2008.
[21] J. Guckenheimer, P. Holmes, Nonlinear Oscillation, Dynamical Systems, and Bifurcations of Vector Fields, Springer-Verlag, New York, 1983.
[22] A. Bulsara, C. Seberino, L. Gammaitoni, M. Karlsson, B. Lundqvist, J.W.C. Robinson, Phys. Rev. E 67 (2003) 016120.
[23] S.A. Campbell, Int. J. Bifur. Chaos 17 (9) (2007) 3109.
[24] H.T. Banks, J.A. Burns, E.M. Cliff, SIAM J. Control Optim. 19 (6) (1981) 791.
[25] D. Yu, M. Frasca, F. Liu, Phys. Rev. E 78 (2008) 046209.
[26] D. Yu, S. Boccaletti, Phys. Rev. E 80 (2009) 036203.